Relativistic electron acceleration by compressional-mode ULF waves: Evidence from correlated Cluster, Los Alamos National Laboratory spacecraft, and ground-based magnetometer measurements

Lun C. Tan,[1] X. Shao,[1] A. S. Sharma,[1] and Shing F. Fung[2]

Received 18 October 2010; revised 15 March 2011; accepted 28 April 2011; published 28 July 2011.

[1] Simultaneous observations by Cluster and Los Alamos National Laboratory (LANL) spacecraft and Canadian Array for Real-Time Investigations of Magnetic Activity and International Monitor for Auroral Geomagnetic Effects magnetometer arrays during a sudden storm commencement on 25 September 2001 show evidence of relativistic electron acceleration by compressional-mode ULF waves. The waves are driven by the quasiperiodic solar wind dynamical pressure fluctuations that continuously buffet the magnetosphere for ~3 h. The compressional-mode ULF waves are identified by comparing the power of magnetic field magnitude fluctuations with the total magnetic field power. The radial distribution and azimuthal propagation of both toroidal and poloidal-mode ULF waves are derived from ground-based magnetometer data. The energetic electron fluxes measured by LANL show modulation of low-energy electrons and acceleration of high-energy electrons by the compressional poloidal-mode electric field oscillations. The energy threshold of accelerated electrons at the geosynchronous orbit is ~0.4 MeV, which is roughly consistent with drift-resonant interaction of magnetospheric electrons with compressional-mode ULF waves.

Citation: Tan, L. C., X. Shao, A. S. Sharma, and S. F. Fung (2011), Relativistic electron acceleration by compressional-mode ULF waves: Evidence from correlated Cluster, Los Alamos National Laboratory spacecraft, and ground-based magnetometer measurements, *J. Geophys. Res.*, *116*, A07226, doi:10.1029/2010JA016226.

1. Introduction

[2] The origin and acceleration of magnetospheric relativistic electrons (MREs) is an outstanding problem in radiation belt physics. There has been increasing evidence indicating the importance of the magnetospheric ULF waves in the Pc-5 frequency range (1–7 mHz) in enhancing MRE flux in the outer belt (see the review of *Elkington* [2006, and references therein]).

[3] Through theoretical analysis and simulation various models have been proposed to explain the acceleration of MREs in terms of their interactions with ULF waves [*Elkington et al.*, 2003; *Degeling et al.*, 2007]. Since electrons drifting in an axially symmetric magnetic field cannot be accelerated by uniformly distributed ULF waves over its drift orbit, asymmetric magnetic field and/or wave distributions are needed for the drift-resonant acceleration mechanism to yield a net energy gain for MREs. For example, *Elkington et al.* [1999, 2003] considered a compressed dipole field model with day-night asymmetry to investigate the acceleration of magnetospheric electrons by both toroidal and poloidal-mode ULF waves. These ULF waves were found to result in electron energization via the drift-resonant interaction.

[4] In this paper, we study compressional poloidal-mode ULF waves and their effects on electron acceleration. The term "compressional poloidal-mode ULF wave" is defined by *Takahashi et al.* [2001] to refer to wave which has the electric field (E_ϕ) and magnetic field (B_z) perturbations and is related to the wave that can transfer wave energy across magnetic field lines. This mode wave is also referred as poloidal-mode wave in this paper. *Degeling et al.* [2007] considered the effect of asymmetric azimuthal distribution of compressional-mode ULF waves on electron acceleration and demonstrated that the compressional poloidal-mode wave is more efficient in electron energization because of azimuthal overlap of the poloidal ULF electric field and electron drift orbit on the dayside of magnetosphere. The azimuthally asymmetric wave distribution can be attributed to the dominance of wave power on the dayside due to the solar wind compression. In addition, *Degeling et al.* [2008] examined the effect of a ULF wave packet with finite duration on electron acceleration. They demonstrated that a burst of narrow band of ULF waves could generate a strong localized peak in the phase space density of MREs because of nondiffusive radial transport of electrons.

[1]Department of Astronomy, University of Maryland, College Park, Maryland, USA.
[2]Geospace Physics Laboratory, NASA Goddard Space Flight Center, Greenbelt, Maryland, USA.

0148-0227/11/2010JA016226

[5] *Tan et al.* [2004] examined the 27 August 1991 sudden storm commencement (SSC) event and observed the correlation between electron acceleration and toroidal-mode ULF waves on the flank. However, the observational evidence of drift-resonant interaction of magnetospheric electrons with compressional-mode ULF waves is limited due to two reasons. First, the resonances with the compressional modes are not localized and the wave power readily spreads through a large volume of space and consequently has small amplitudes [*Kivelson*, 2006]. Second, the drift-resonant interaction between compressional-mode ULF waves and MREs is cumulative over the MRE drift orbit. One possible way of finding evidences of resonant acceleration of MREs is to analyze simultaneous observations from multispacecraft and ground-based magnetometer arrays covering a large L range in the outer radiation belt.

[6] This paper presents evidence of relativistic electron acceleration by the compressional-mode ULF waves during a SSC on 25 September 2001 in the observations by four Cluster spacecraft measuring ULF waves and low-energy electron flux, and five LANL spacecraft measuring energetic electron fluxes over a wide energy range. The progenitor of the 25 September 2001 SSC event was the 24 September 2001 solar energetic particle (SEP) event examined by *Tan et al.* [2009]. The primary coronal mass ejection (CME) that caused the SEP event was launched at 1016 UT of 24 September and the interplanetary shock driven by the CME arrived at Earth at 2025 UT of 25 September, leading to a powerful (8A + 2B + 2C) SSC event. The Wind and Geotail spacecraft monitoring the upstream solar wind measured a speed of 670 km^{-1} behind the shock. Also, at the beginning of SSC event the geomagnetic indices were $Kp = 6$ and $AE = 1100$ nT.

[7] During the event, the Cluster spacecraft were near their perigee (see Figure 1) and the duskward electric field component (E_y) measured by them are close to E_φ, and is useful for investigating the electron acceleration by poloidal-mode ULF waves. During the event interval both LANL and GOES spacecraft detected a significant enhancement of MREs. The Canadian Array for Real-Time Investigations of Magnetic Activity (CARISMA) [*Mann et al.*, 2008] magnetometer array was near noon, approximately in a conjunction with GOES 8 and LANL91 spacecraft, while the International Monitor for Auroral Geomagnetic Effects (IMAGE) magnetometer array was near midnight. Both arrays provided ground magnetometer data of the event.

[8] In this paper, we address the following aspects on the MRE acceleration by ULF waves through the analysis of the 25 September 2001 event.

[9] 1. During this event, magnetospheric ULF waves were excited by solar wind fluctuations, as shown by their correlation with solar wind dynamic pressure fluctuations. The waves were excited by solar wind quasiperiodic pulsations, similar to those found by *Kim et al.* [2002].

[10] 2. The presence of compressional-mode ULF waves during the event was identified by measuring the power spectral densities of various magnetic field components. The radial distribution and azimuthal propagation of both toroidal and poloidal-mode ULF waves are derived from ground-based magnetometer data.

[11] 3. The time scale of MRE acceleration during the event is about several hours, and consequently the electron acceleration cannot be due to the radial diffusion [e.g., *Schulz and Lanzerotti*, 1974], which needs an acceleration time scale of days [*Elkington et al.*, 2003]. Also, the impulsive electron acceleration due to strong sudden dayside magnetosphere compression by fast interplanetary shocks that last for only a few minutes (e.g., during the 24 March 1991 SSC event [see *Blake et al.*, 1992; *Li et al.*, 1993]) is insufficient to explain the acceleration time scale in the 25 September 2001 event.

[12] In the next section we present the data from Cluster, LANL, GOES, Geotail, and Wind spacecraft and the ground-based magnetic field data provided by the CARISMA and IMAGE magnetometer arrays. In section 3, we report the observational characteristics of Pc-5 ULF waves during the 25 September 2001 SSC event. In section 4, we describe the observed dynamics of magnetospheric relativistic electrons, followed by analysis and theory on the electron acceleration by ULF waves in section 5.

2. Spacecraft and Ground Magnetometer Data Sources

[13] The 25 September 2001 SSC event was monitored by Cluster quartet, LANL90, 91, 94, 97, and 01, and GOES 8 and 10 spacecraft (Figure 1). For the event (2000–2100 UT on 25 September 2001) we use colored dots and arrows to denote the spacecraft orbit and motion direction, respectively, in Figure 1. The solid lines in Figure 1 denote the orbit of Cluster quartet over a longer interval, during which the spacecraft traveled from night side to the perigee near noon and back to night side, while the dotted line is the magnetic field line traced through Cluster-3 at 2030 UT using the Tsyganenko T89 model [*Tsyganenko*, 1989], indicating an orbit conjunction between Cluster-3 and LANL91. This conjunction enables us to compare the electric field and electron flux measurements between the two spacecraft.

[14] The Cluster Electric Field and Wave (EFW) instrument [*Gustafsson et al.*, 1997] provides the electric field vector **E** data. Since Cluster was near noon during the September event, we can approximate the Cluster E_y(GSE) component to E_ϕ. Also, we use the magnetic field vector **B** data obtained by the Cluster Fluxgate magnetometer (FGM) [*Balogh et al.*, 1997] and low-energy electron data obtained by the RAPID instrument [*Rème et al.*, 2001] in our analysis.

[15] The Los Alamos National Laboratory (LANL) Synchronous Orbit Particle Analyzer (SOPA) [*Belian et al.*, 1992] provides the omnidirectional electron flux (J_e) data over a wide electron kinetic energy (E_e) range (50 keV–1.5 MeV). All LANL spacecraft carried the same instrument, making it easy to quantitatively compare electron fluxes measured on different LANL spacecraft. As shown in Figure 1, these 5 LANL spacecraft were nearly uniformly distributed in the azimuthal direction, among which LANL01, 97, and 94 were located on the night side, LANL91 was close to noon, and LANL90 was located at dusk. Also, the GOES spacecraft [*Singer et al.*, 1996] provides the magnetic field and high-energy electron flux data.

[16] The upstream solar wind environment is monitored by the Wind and Geotail spacecraft. In this work we use data from the Solar Wind Experiment (SWE) [*Ogilvie et al.*, 1995] on Wind spacecraft, and the Magnetic Field (MGF) instrument [*Kokubun et al.*, 1994] and low-energy particle (LEP) instrument [*Mukai et al.*, 1994] on Geotail spacecraft. During

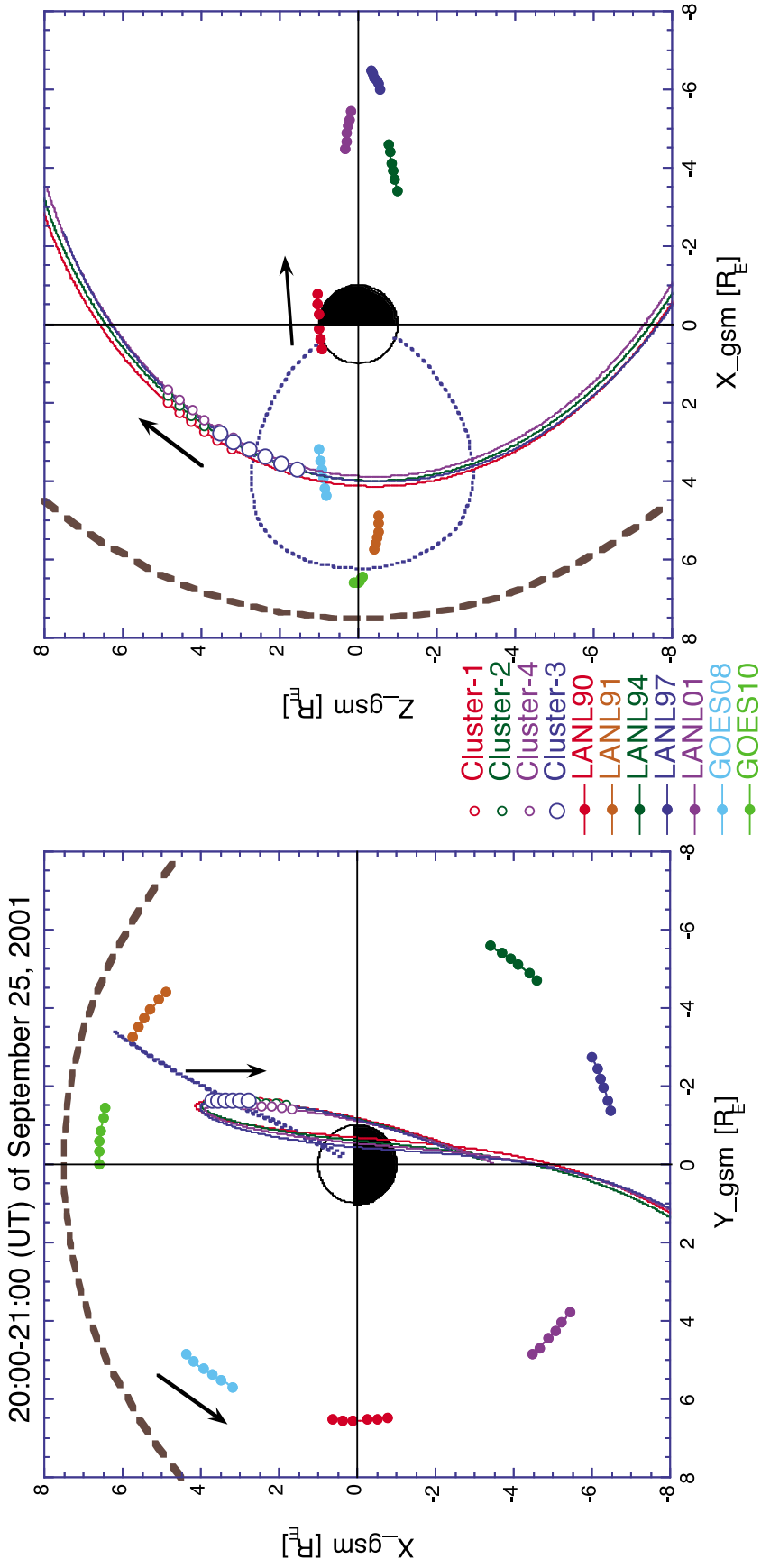

Figure 1. Spacecraft orbits during the sudden storm commencement (SSC) event period (2000–2100 UT on 25 September 2001). The arrows indicate the direction of spacecraft motion. The solid lines are the Cluster orbits over a 2 day interval. The dotted line is the magnetic field line traced through Cluster-3 at 2030 UT using the T89 model. The dashed line is the estimated magnetopause location.

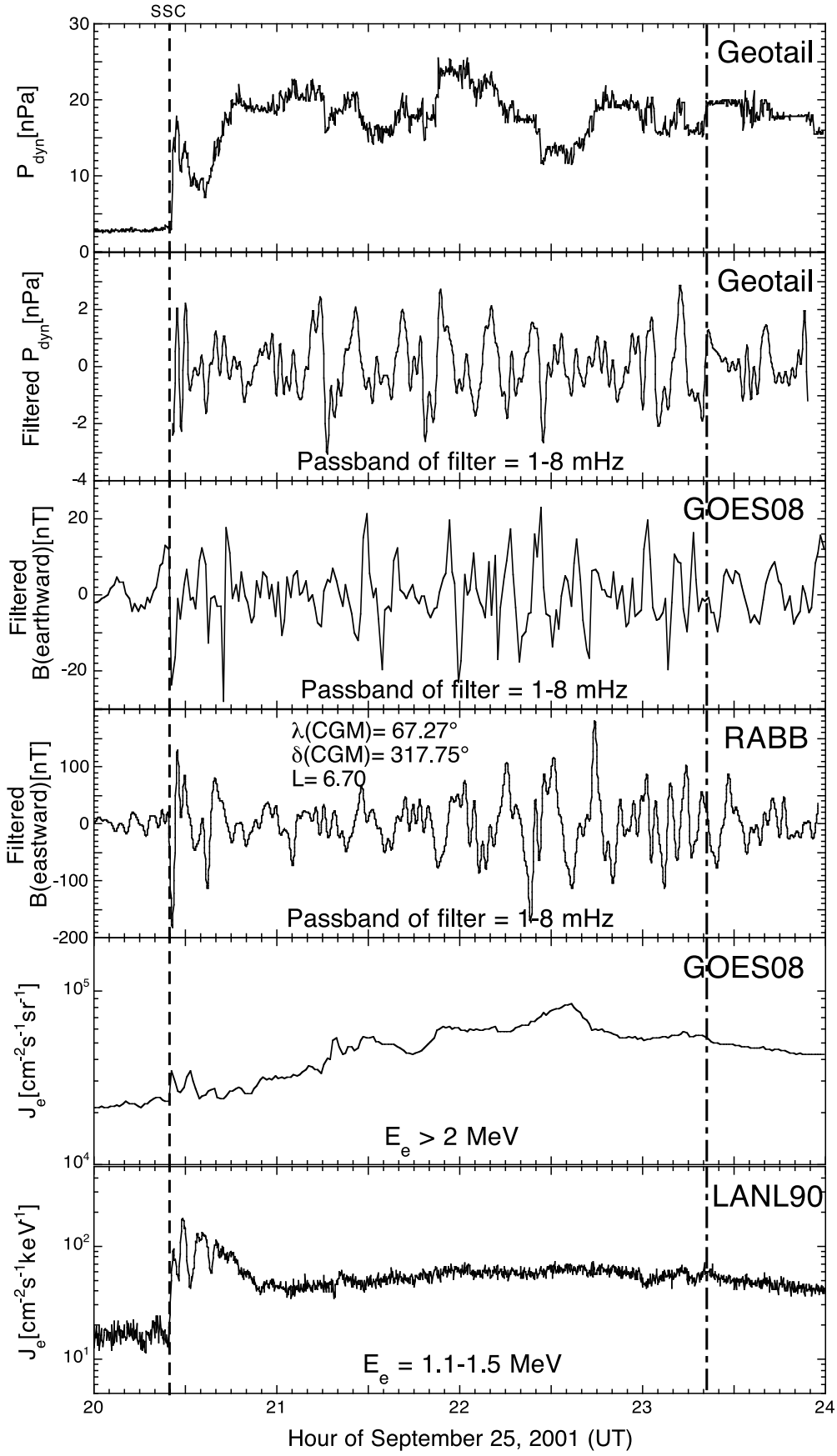
SSC
Geotail
P_{dyn} [nPa]
Geotail
Filtered P_{dyn} [nPa]
Passband of filter = 1-8 mHz
GOES08
Filtered B(earthward)[nT]
Passband of filter = 1-8 mHz
λ(CGM)= 67.27°
δ(CGM)= 317.75°
L= 6.70
RABB
Filtered B(eastward)[nT]
Passband of filter = 1-8 mHz
GOES08
J_e[cm^{-2}s^{-1}sr^{-1}]
E_e > 2 MeV
LANL90
J_e[cm^{-2}s^{-1}keV^{-1}]
E_e = 1.1-1.5 MeV
Hour of September 25, 2001 (UT)

Figure 2

the event interval Geotail was located at X(GSE) = 11.7, Y(GSE) = −17.1, and Z(GSE) = −0.5 R_E (R_E is the Earth's radius), i.e., near the magnetopause but still in the interplanetary space. Consequently, we can compare the Geotail data with magnetospheric observations without any correction of solar wind time delay.

[17] In addition to the spacecraft observations, we use the ground-based magnetic field measurements obtained by the CARISMA (the continuation of CANOPUS [*Rostoker et al.*, 1995]) magnetometer array (see http://portal.cssdp.ca:8080/ssdp/jsp/logon.jsp) and the IMAGE magnetometer array (see http://www.ava.fmi.fi/image/data.html). The Corrected Geomagnetic Coordinates (CGM) of ground stations are calculated from the NASA/Space Physics Data Facility (SPDF) website (see http://omniweb.gsfc.nasa.gov/vitmo/cgm_vitmo.html).

3. Observed ULF Wave Characteristics

3.1. Upstream Solar Wind Conditions

[18] In order to check if the magnetospheric Pc-5 ULF waves were driven by the solar wind dynamic pressure fluctuations as suggested by *Kim et al.* [2002] and *Kepko et al.* [2002], we plot in Figure 2 the time profiles of solar wind dynamical pressure, magnetospheric ULF wave amplitude, and geosynchronous MRE fluxes. The Geotail observations (Figure 2, first panel) show an increased solar wind dynamic pressure P_{dyn} after the SSC. The filtered P_{dyn} with a passband filter of 1–8 mHz (the frequency range of the main poloidal electric field power; see Figure 3) is shown in Figure 2 (second panel), where high P_{dyn} oscillations lasted until 2320 UT. The filtered poloidal magnetic field components measured by GOES 8 (B_r; Figure 2, third panel) and by the CARISMA RABB magnetometer (B(eastward); Figure 2, fourth panel) show a time variation similar to that found in the solar wind P_{dyn}: large amplitude perturbations in the Pc-5 wave frequency range also lasted until ~2320 UT. Note that in the CARISMA magnetometer array RABB was closest to GOES 8 at local time during the event interval.

[19] On the other hand, after the first rapid rise that is probably due to the impulsive electron acceleration by the sudden dayside magnetosphere compression like in the 24 March 1991 SSC event [*Blake et al.*, 1992; *Li et al.*, 1993], the MRE fluxes measured by GOES (Figure 2, fifth panel) and LANL (Figure 2, sixth panel) spacecraft show a gradual increase until ~2320 UT, after which the fluxes decrease with time. The event is hence different from the minute time scale impulsive MRE acceleration during the 24 March 1991 SSC event [*Blake et al.*, 1992; *Li et al.*, 1993] because of the necessity to introduce additional electron acceleration during a relatively long (~3 h) time interval. Since the durations of solar wind dynamic pressure fluctuations and magnetospheric ULF waves were aligned well with the electron acceleration period (i.e., 2025–2320 UT, between the vertical dashed and dash-dotted lines in Figure 2), it is useful to study the linkage among the electron acceleration and the ULF waves driven by solar wind dynamic pressure fluctuations, as presented in following sections. More importantly, the phase correlation between the solar wind dynamic pressure fluctuations observed by Geotail and the magnetospheric ULF waves observed by GOES 8 as described later in Figure 8 is in support of the ULF waves driven by the solar wind dynamic pressure fluctuations.

3.2. Characteristics of Compressional-Mode ULF Waves in the Magnetosphere

[20] According to the magnetospheric cavity/waveguide model [*Zhu and Kivelson*, 1988; *Mann and Wright*, 1999; *Kivelson*, 2006], compressional-mode waves, generated near the magnetopause, propagate across the magnetic field lines toward the Earth. The increase in Alfvén speed with magnetic field strength as radial distance is decreased leads to the reflection of these waves along a boundary within the magnetosphere, known as a cutoff or turning point. Compressional-mode oscillations earthward of the turning point are evanescent. An important characteristic of compressional-mode waves is that it supports harmonic oscillations across substantial radial distances inside the magnetosphere.

[21] Figure 3 shows the frequency spectra of power spectral densities (PSDs) of the Wind solar wind dynamic pressure (P_{dyn}; Figure 3, first panel), Geotail solar wind dynamic pressure (P_{dyn}; Figure 3, second panel), GOES 8 (Figure 3, third panel), CARISMA RABB (Figure 3, fourth panel), and Cluster-3 magnetic field, and Cluster-3 poloidal electric field component (E_ϕ; Figure 3, sixth panel). Figure 3 hence samples the solar wind driving process from Wind to Cluster-3 spacecraft. Note that among the Cluster quartet only Cluster-3 detected ULF waves with large amplitudes because of its unique location (at L = 5–12) during the event interval. In fact, after 2100 UT the rapid decrease of ULF wave amplitudes seen by Cluster-3 is due to the spacecraft having entered the high-latitude nightside region. From Figure 3 it can be seen that the observed ULF wave frequency spectra are of wide band with multiple peaks. Since E_ϕ mainly causes the electron acceleration, from Figure 3 (sixth panel), we find that E_ϕ has a broad maximum within the frequency range of 1–8 mHz (the shaded gray region). During the entire solar wind driving process we see broadband ULF oscillations existing at all observation points.

[22] In addition, in Figure 3 we define PSD(B_{tot}) and PSD(B_{mag}) to express the total magnetic field power (the sum of PSDs for three magnetic field components) and the power of magnetic field magnitude, respectively. Since within the shaded gray region the PSD ratio of B_{tot} to B_{mag} is between ~1 for GOES 8 and ~10 for Cluster-3, the amplitude of B_{mag} oscillations is comparable to that of any magnetic field component. Therefore, the observed ULF waves are compressional in nature.

Figure 2. Time profiles of the solar wind dynamical pressure P_{dyn} measured by Geotail (first panel), filtered P_{dyn} measured by Geotail (second panel), filtered magnetic field B(earthward) component measured by GOES 8 (third panel), filtered magnetic field B(eastward) component measured by CARISMA RABB station (fourth panel), and magnetospheric relativistic electron (MRE) fluxes measured by GOES 8 (fifth panel) and by LANL (sixth panel) spacecraft. The dash-dotted line indicates the end time of electron acceleration. A broadband (1–8 mHz) filter is applied to P_{dyn} and B data.

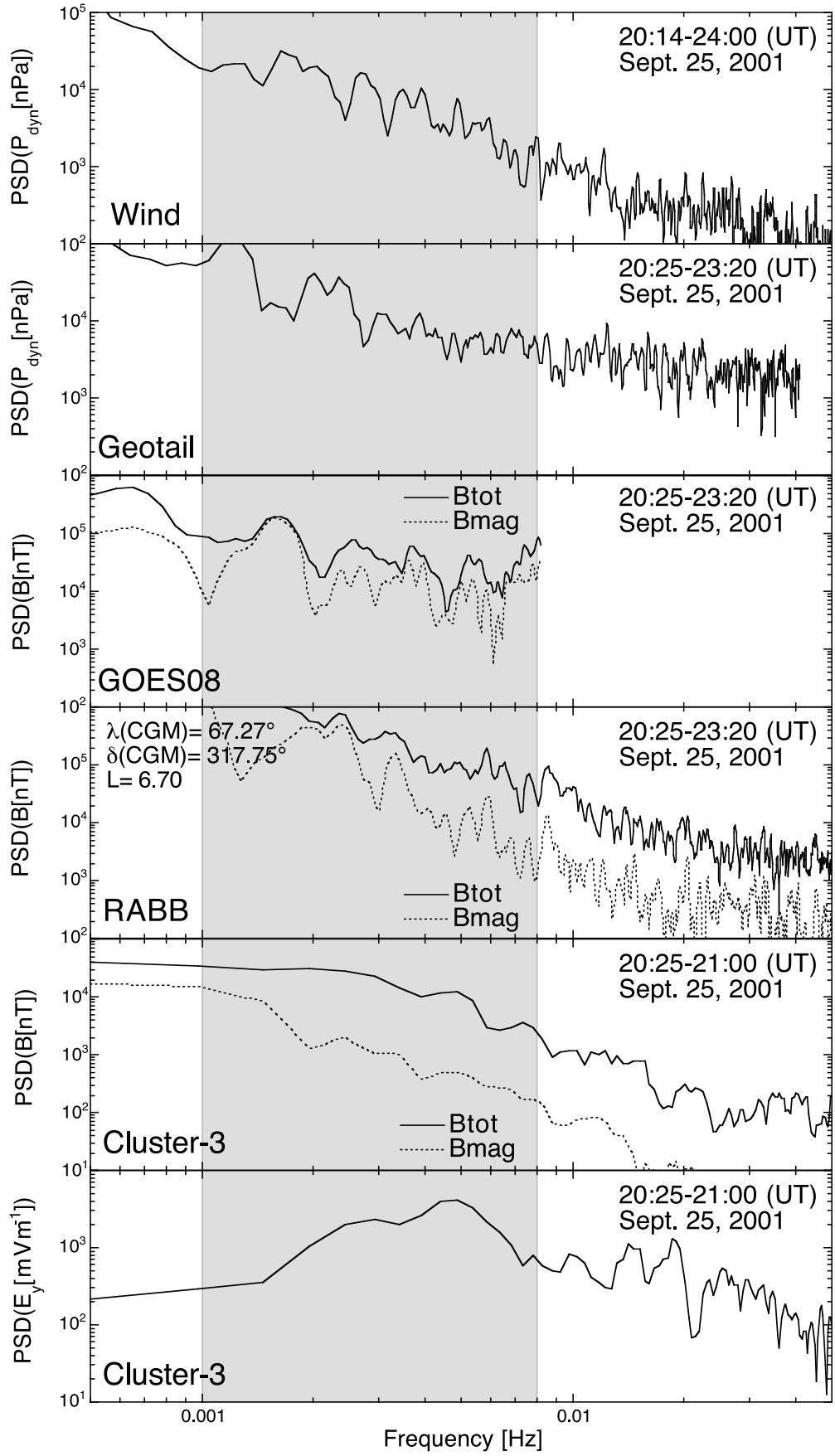
20:14-24:00 (UT)
Sept. 25, 2001
Wind
PSD(P_dyn[nPa])
20:25-23:20 (UT)
Sept. 25, 2001
Geotail
PSD(P_dyn[nPa])
Btot
Bmag
20:25-23:20 (UT)
Sept. 25, 2001
GOES08
PSD(B[nT])
λ(CGM)= 67.27°
δ(CGM)= 317.75°
L= 6.70
20:25-23:20 (UT)
Sept. 25, 2001
RABB
Btot
Bmag
PSD(B[nT])
20:25-21:00 (UT)
Sept. 25, 2001
Cluster-3
Btot
Bmag
PSD(B[nT])
20:25-21:00 (UT)
Sept. 25, 2001
Cluster-3
PSD(E_y[mVm^-1])
0.001
0.01
Frequency [Hz]

Figure 3

[23] Because of the frequency range of ULF waves involved in this event, below we will use the broad band (1–8 mHz) and narrow band (3–5 mHz) filters in the examination of acceleration power and phase relation of ULF waves, respectively.

3.3. Characteristics of ULF Waves Observed by Ground-Based Magnetometers

3.3.1. CARISMA Magnetometer Observations Along Fort Churchill Line

[24] Magnetic field data of five CARISMA magnetometer stations along the Fort Churchill (FCHU) line are shown in Figure 4, where the stations have similar longitudes but different latitudes. The maximum of latitudinal separation is $\Delta\lambda(\mathrm{CGM}) = 11°$, which corresponds to the L difference of 4.4, where L is the dipolar L as defined by $L = 1/\cos^2(\lambda(\mathrm{CGM}))$. In Figure 4 the magnetic field B(northward) and B(eastward) components filtered by a broadband (1–8 mHz) filter are shown. It can be seen that the amplitudes of the two components were large at high-L stations, but drastically decreased at $L < 6$. In addition, at high-L stations (ESKI and FCHU) the wave amplitude also rapidly decreased after 2320 UT as indicated by the dash-dotted line (also see Figure 2), while at low-L stations, no such decreasing tendency was seen. The radial distribution of ULF waves is consistent with that the compressional-mode waves earthward of the turning point are evanescent. The ULF wave oscillations at larger L can be driven by the solar wind fluctuations. In section 5.1, we will deduce the equatorial electric field amplitude of ULF waves based on these ground-based magnetometer measurements.

3.3.2. Comparison of Magnetometer Observations Between RABB and DAWS Stations of CARISMA

[25] The RABB and DAWS stations have similar latitudes (i.e., L values) but different longitudes, with the longitudinal separation of $\Delta\delta = 35.43°$ (see Figure 5, first panel). The magnetometer data measured at longitudinally separated stations can be used to estimate the azimuthal propagation of ULF waves. In low-beta plasma such as in the magnetosphere, the fast-mode wave propagation speed across the magnetic field line is close to Alfvén speed. It has been shown that the azimuthal wave number measured by using various wave components would be same [e.g., *Olson and Rostoker*, 1978, and references therein]. For example, *Olson and Rostoker* [1978] examined 61 relatively uncontaminated Pc 4–5 micropulsations and found that the azimuthal wave numbers deduced from H (N–S) component and D (E–W) component agreed in both magnitude and sign (see their Figure 3). However, usually the H component is stronger and more stable. We thus use the H component to determine the m value.

[26] Time profiles of the B(northward) (H component) filtered by a narrowband (3–5 mHz) filter are shown for the two stations in Figure 5 (second panel), where the phase difference of waves between the two stations can be seen. Note that the first two successive pulses have opposite sign, with negative/positive (positive/negative) polarity at RABB (DAWS), which is consistent with the B(northward) signal commonly observed at auroral latitudes, where in the morning a positive pulse typically precedes and a negative pulse follows, while the sense of the pulses is reversed in the afternoon [*Villante et al.*, 2006]. After 1.5 wave periods, however, a wave phase difference less than $\pi/2$ stably existed between RABB and DAWS for ~1 h. The sign of phase difference indicates that the wave propagated westward from RABB to DAWS (see Figure 5, first panel).

[27] We have chosen 8 continuous wave periods starting from 20.9 h (UT) to estimate the wave phase difference $\Delta\phi$ between RABB and DAWS, from which we calculate the azimuthal wave number m. According to *Olson and Rostoker* [1978],

$$m = \Delta\phi/\Delta\delta. \tag{1}$$

The wave phase difference can be expressed as

$$\Delta\phi = 360\Delta t/\tau_w, \tag{2}$$

where Δt is the difference of wave arrival times between the two stations and τ_w is the wave period. Thus we have

$$m = \Delta\phi/\Delta\delta = 360\Delta t/(\tau_w\Delta\delta). \tag{3}$$

Substituting $\Delta t = 0.025 \pm 0.005$ h, $\tau_w = 0.079 \pm 0.010$ h, and $\Delta\delta = 35.43°$ into equation (3), we obtain $m = 3.2 \pm 0.8$ (i.e., $m \sim 3$). In addition, in order to test the stability of our deduced m value, we repeated the m calculation by using a broadband (1–8 mHz) filter (see Figure 5, fourth panel). We found that $\Delta t = 0.019 \pm 0.005$ h and $\tau_w = 0.057 \pm 0.014$ h. Thus we obtained $m = 3.3 \pm 1.2$, which is consistent with that deduced from the narrowband (3–5 mHz) filter data.

3.3.3. Comparison of Magnetometer Observations Between LEK and LOZ Stations of IMAGE

[28] During the 25 September 2001 SSC event interval the IMAGE magnetometer array was located near midnight (see Figure 5, first panel). Among IMAGE magnetometers LEK and LOZ have similar latitudes but a longitudinal separation of $\Delta\delta = 21.54°$. In Figure 6 we show the time profiles of B(northward) oscillations observed by LEK and LOZ as filtered by a narrowband (3–5 mHz) filter. The phase difference of waves between the two stations was very small. However, except the intervals with nonsine waveforms, the wave observed at LEK stably preceded that at LOZ, indicating the eastward propagating waves along the dusk flank. Substituting $\Delta t = 0.0035 \pm 0.0016$ h, $\tau_w = 0.062 \pm 0.005$ h, and $\Delta\delta = 21°.54$ into equation (3), we obtain $m = 0.9 \pm 0.4$ (i.e., $m \sim 1$). Surprisingly, we observe a large difference of azimuthal wave numbers between noon and midnight. When a broadband (1–8 mHz) filter was used, however, we noted that clear peak of waves could not be recognized, especially

Figure 3. Frequency spectra of power spectral densities (PSDs) of the solar wind dynamic pressure P_{dyn} from Wind (first panel) and from Geotail (second panel), the magnetic field (B_{tot} and B_{mag}) from GOES 8 (third panel), CARISMA RABB station (fourth panel), and Cluster-3 (fifth panel), and the poloidal electric field (E_y) from Cluster-3 (sixth panel). PAD (B_{tot}) and PSD (B_{mag}) are defined to express the total magnetic field power (the sum of PSDs for three magnetic field components) and the power of the magnetic field magnitude, respectively. The shaded region covers the main power range of E_y in Figure 3 (sixth panel). The data sampling interval is shown in the upper right corner in each panel.

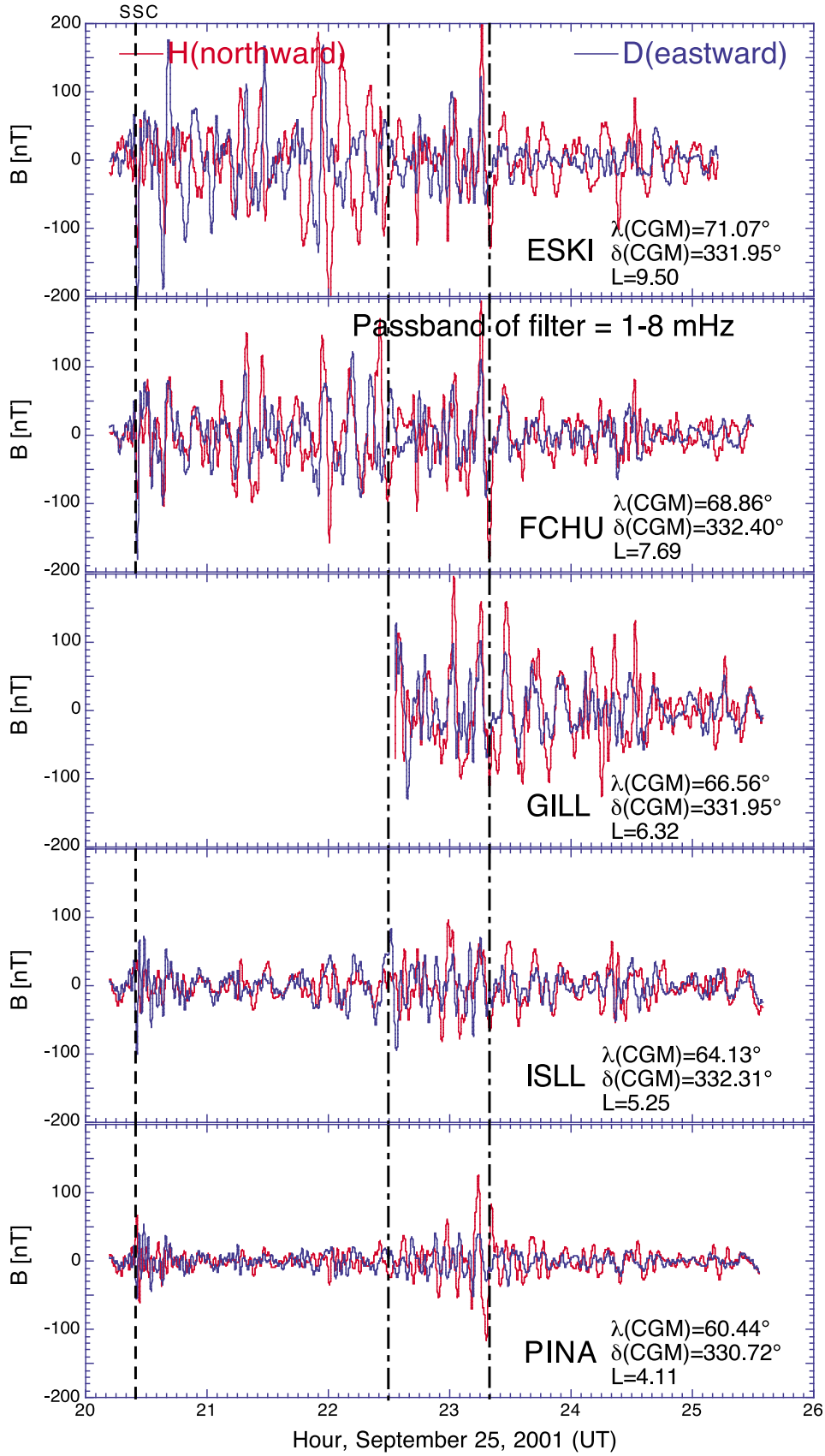

Figure 4. Time profiles of the magnetic field *B*(northward) and *B*(eastward) components measured by the CARISMA Fort Churchill (FCHU) line magnetometer array. The field components are filtered by a broadband (1–8 mHz) filter. The right dash-dotted line indicates the stop time of electron acceleration.

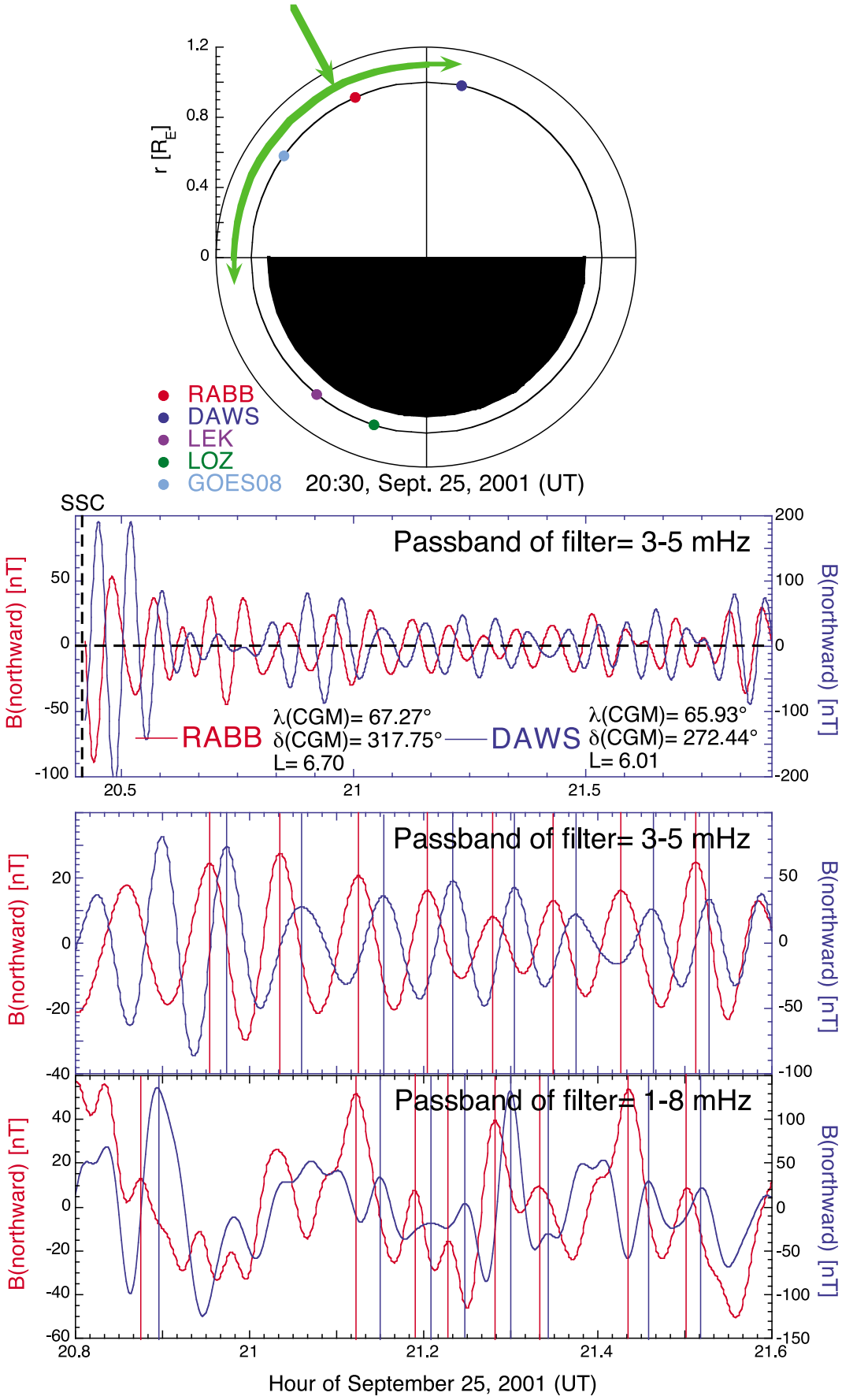
r [R_E]
1.2
0.8
0.4
0
RABB
DAWS
LEK
LOZ
GOES08
20:30, Sept. 25, 2001 (UT)
SSC
Passband of filter= 3-5 mHz
B(northward) [nT]
RABB
λ(CGM)= 67.27°
δ(CGM)= 317.75°
L= 6.70
DAWS
λ(CGM)= 65.93°
δ(CGM)= 272.44°
L= 6.01
Passband of filter= 3-5 mHz
Passband of filter= 1-8 mHz
Hour of September 25, 2001 (UT)

Figure 5

from LOZ data (see Figure 9, sixth panel). We cannot estimate the m value from the broadband filter data.

3.3.4. Comparison of ULF Wave Amplitudes Between CARISMA and IMAGE Magnetometer Arrays

[29] Because of the preferable locations of both CARISMA (near noon) and IMAGE (near midnight) magnetometer arrays during the 25 September 2001 event interval, it is interesting to check if the ULF wave amplitudes measured by the two arrays are different. The average amplitudes of ULF oscillations deduced from the both arrays as filtered by a broadband (1–8 mHz) filter are shown in Figure 7 (top and middle) for the northward and eastward magnetic field components, respectively. For the CARISMA data, at $L < 6$ both B(northward) and B(eastward) amplitudes increase with increasing L, while an amplitude plateau with a shallow maximum near $L \sim 6.5$ appears at $L > 6$, which is consistent with *Vassiliadis et al.* [2007] who observed that the ground ULF wave power has a peak in the range $3.5 < L < 6.4$ and distributed uniformly in the range $6.4 < L < 15$. Furthermore, at $L < 5.5$ the wave amplitude measured by IMAGE is consistent with that by CARISMA. Since the wave amplitudes measured at noon and midnight are similar, the observed absence of $m = 3$ waves near midnight implies a significant asymmetry of $m = 3$ mode wave components between noon and midnight.

3.4. Phase Comparison Between Solar Wind Dynamical Pressure Fluctuations and Magnetospheric Poloidal-Mode Waves

[30] Furthermore, it is interesting to examine if there exists a phase correlation between the solar wind dynamical pressure (P_{dyn}) oscillations observed on Geotail and the poloidal magnetic field oscillations (B_r) observed on GOES 8. Time profiles of Geotail P_{dyn} and GOES 8 B_r fluctuations as filtered by a narrowband (3–5 mHz) filter are shown in Figure 8, where after the first two wave periods the phase difference between the two oscillations is nearly unchanged.

[31] Assuming that the phase difference between the Geotail P_{dyn} and GOES 8 B_r fluctuations is due to the azimuthal propagation effect of ULF waves from impinging location of the solar wind at the magnetopause to GOES 8, we can determine at the azimuthal location at the magnetopause where the solar wind impinges the magnetosphere. By substituting $\Delta t = 0.017 \pm 0.003$ h, $\tau_w = 0.071 \pm 0.005$ h, and $m = 3.2 \pm 0.8$ into equation (3) we can estimate the longitudinal difference $\Delta\delta = 27 \pm 8°$ between GOES 8 and the impinging location of the solar wind at the magnetopause, shown in Figure 5 (first panel) as the green arrow. In addition, we also estimated $\Delta\delta$ by using a broadband (1–8 mHz) filter (see Figure 8, bottom). From our measured $\Delta t = 0.011 \pm 0.003$ h and $\tau_w = 0.042 \pm 0.006$ h, we obtained $\Delta\delta = 28 \pm 11°$, which is also consistent with that deduced from the narrowband (3–5 mHz) filter data.

[32] Therefore, the analysis of Geotail, GOES 8, CARISMA, and IMAGE data consistently indicate that the solar wind buffeting region (i.e., the source of the observed ULF waves) may be located in the afternoon sector, explaining the different phase propagation directions toward morning and toward dusk as described by the phase differences between Geotail and GOES 8, between RAB and DAWS, and between LEK and LOZ, respectively. It should be emphasized that along the dusk flank the antisunward propagating waves are important, because they could resonantly interact with and accelerate the electrons. This explains why the most significant electron acceleration is observed at dusk by LANL90 spacecraft.

[33] There have been several mechanisms to excite magnetospheric ULF wave oscillations by solar wind dynamic pressure changes.

[34] 1. ULF harmonic oscillations in solar wind dynamic pressure can be directly transmitted into the magnetosphere and the ULF magnetic field fluctuations show spectral peaks corresponding to driver frequency peaks in the solar wind dynamic pressure. An example of this type of excitation is the case shown by *Kepko et al.* [2002].

[35] 2. Abrupt changes such as shock wave or CMEs in the solar wind can have sudden and/or steplike increases dynamic pressure and can excite ULF magnetospheric waves. The magnetosphere is compressed and broadband fast mode waves may be launched because of the impulsive nature of the source. Such fast mode waves are then coupled to local standing Alfvén waves through the field line resonance process. An example this type of excitation is shown by *Kim et al.* [2002] and *Zong et al.* [2009]. In *Zong et al.* [2009], less than 1 h of ULF wave oscillations were observed in two events after the shock-related solar wind pressure pulse.

[36] 3. When the solar wind dynamic pressure changes quasiperiodically (buffeting), the magnetopause is driven so that the magnetospheric magnetic field is perturbed through compressional-mode wave excitation. The field perturbations are complicated at higher latitudes ($L = 2.9$–6.1) on the dayside. In particular, the frequency peaks of electric and magnetic signals observed inside the magnetosphere may be at the resonant frequency of cavity mode oscillations, which may not be same as their corresponding driver frequencies in the solar wind. The duration of this kind of excitation can last several hours. An example this type of excitation is shown by *Kim et al.* [2002].

[37] 4. With stable high speed solar wind and northward IMF, Kelvin-Helmholtz instability at the flank side magnetopause caused ULF magnetopause oscillations, which coupled energy to standing Alfvén waves propagating along the resonant field lines. An example this type of excitation is shown by *Rae et al.* [2005].

[38] In this event, based on the same ~3 h buffeting time interval of solar wind pressure and magnetospheric ULF wave excitation (Figure 2) and the phase correlation between the (Geotail) solar wind pressure and (GOES 8) magnetic field wave power (Figure 8) we believe that the

Figure 5. Local time distribution of ground magnetometer stations and GOES 8 used in the wave phase analysis of the 25 September 2001 SSC event, where the green arrow indicates the buffeting place of the solar wind on the magnetosphere (first panel). Filtered (3–5 mHz bandwidth) time profiles of B(northward) components measured by CARISMA RABB and DAWS stations, whose CGM coordinates are shown on the lower right corner (second panel). Expanded views in time scale for time profiles of B(northward) components filtered using two filters with 3–5 mHz (third panel) and 1–8 mHz (fourth panel) bandwidth. The vertical lines indicate the wave peak crossing time.

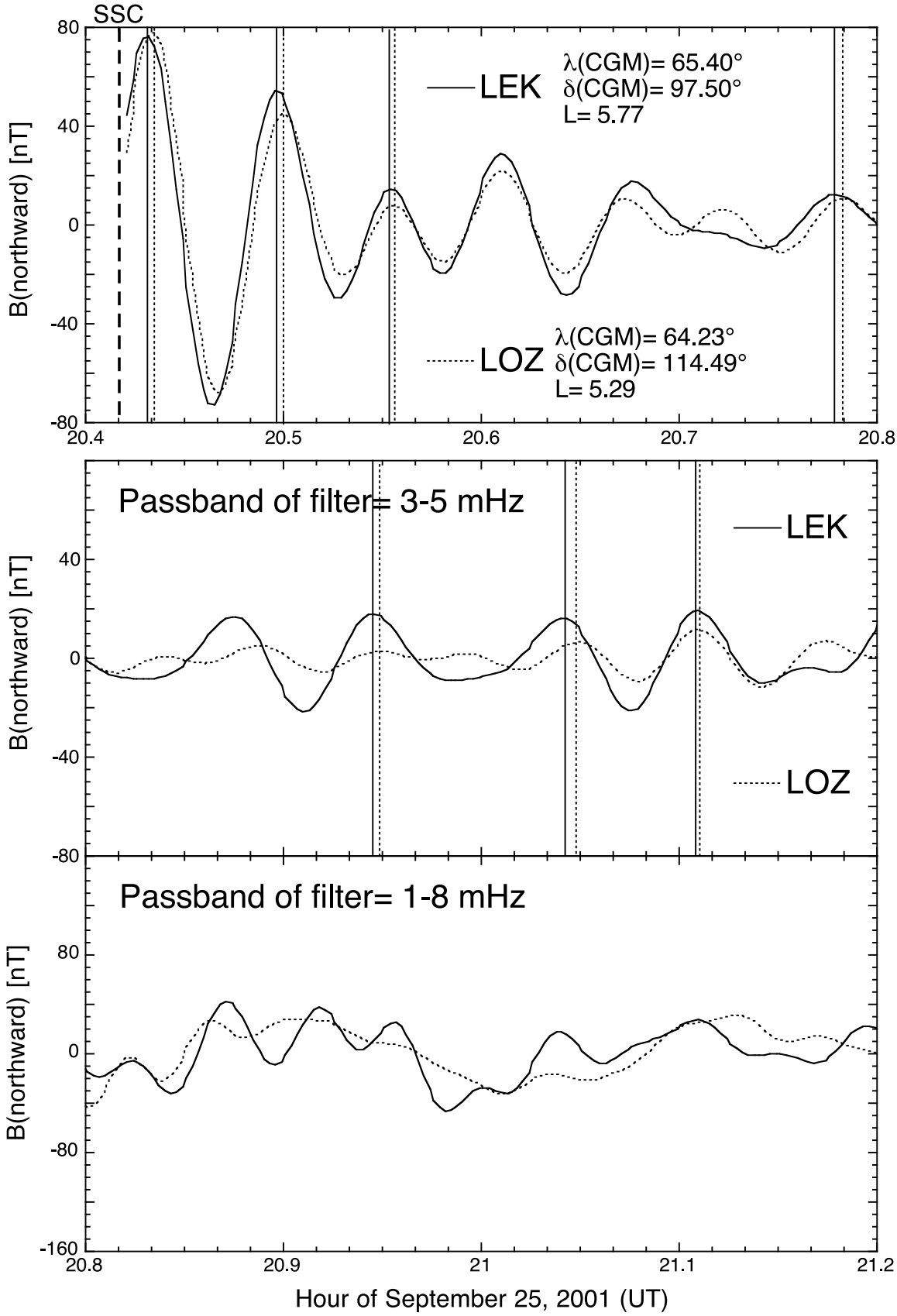

Figure 6. Time profiles of *B*(northward) components measured by IMAGE LEK and LOZE stations. The vertical lines indicate the wave peak crossing time. (top and middle) A narrowband (3–5 mHz) filter is used. (bottom) A broadband (1–8 mHz) filter is used.

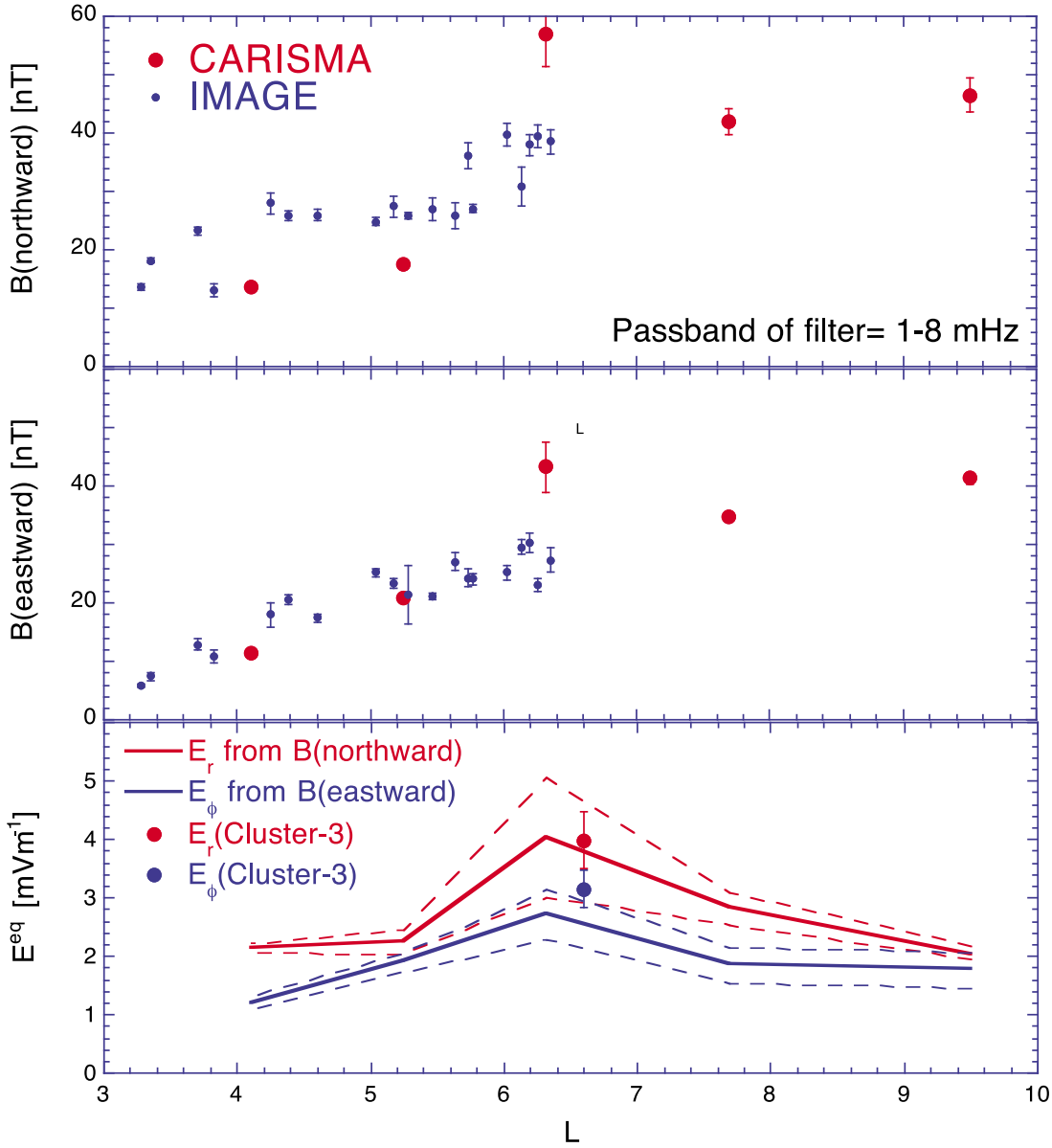

Figure 7. The average amplitudes of (top) B(northward) and (middle) B(eastward) components measured by CARISMA and IMAGE magnetometer arrays as filtered by a broadband (1–8 mHz) filter. (bottom) The equatorial electric field E_{eq} values deduced from the FCHU line magnetometer array (solid line) and Cluster-3 (dots) data are plotted against L for both toroidal (E_r) and poloidal (E_φ) mode waves. The dashed lines show the estimated error ranges of E_{eq}.

ULF waves are driven by continuous buffeting of the solar wind dynamical pressure variation, which is similar to the type of excitation presented by *Kim et al.* [2002].

4. Observed Dynamics of Magnetospheric Relativistic Electrons

4.1. Modulation of Low-Energy Electron Fluxes

[39] The modulation of low-energy electron fluxes by the poloidal-mode electric field (E_ϕ) is shown in Figure 9, where the time profiles of E_ϕ measured by Cluster-3 and J_e measured by Cluster-3 and LANL91 spacecraft as filtered by a broad band (1–8 mHz) filter are shown. The Cluster-3 differential flux J_e is deduced from its integrated flux data $f(E > E_0)$ provided by Cluster RAPID data, i.e., $J_e = f(E > 30\ \text{keV}) - f(E > 100\ \text{keV})/(100\ \text{keV} - 30\ \text{keV})$, which gives the differential electron fluxes at the electron energy deduced from spectral mean.

[40] Because of the conjunction between Cluster-3 and LANL91 orbits, i.e., being connected through nearby magnetic field lines, the peaks of the omnidirectional electron flux J_e (for electron energy <100 keV) measured on the two spacecraft are aligned to each other very well. In Figure 9 the vertical thin lines mark the time when E_ϕ measured by Cluster-3 crosses zero from negative to positive. These vertical lines are well aligned with the low-energy electron (<100 keV) flux (J_e) peaks measured on both Cluster-3 and LANL91 spacecraft, indicating the coherent wave modula-

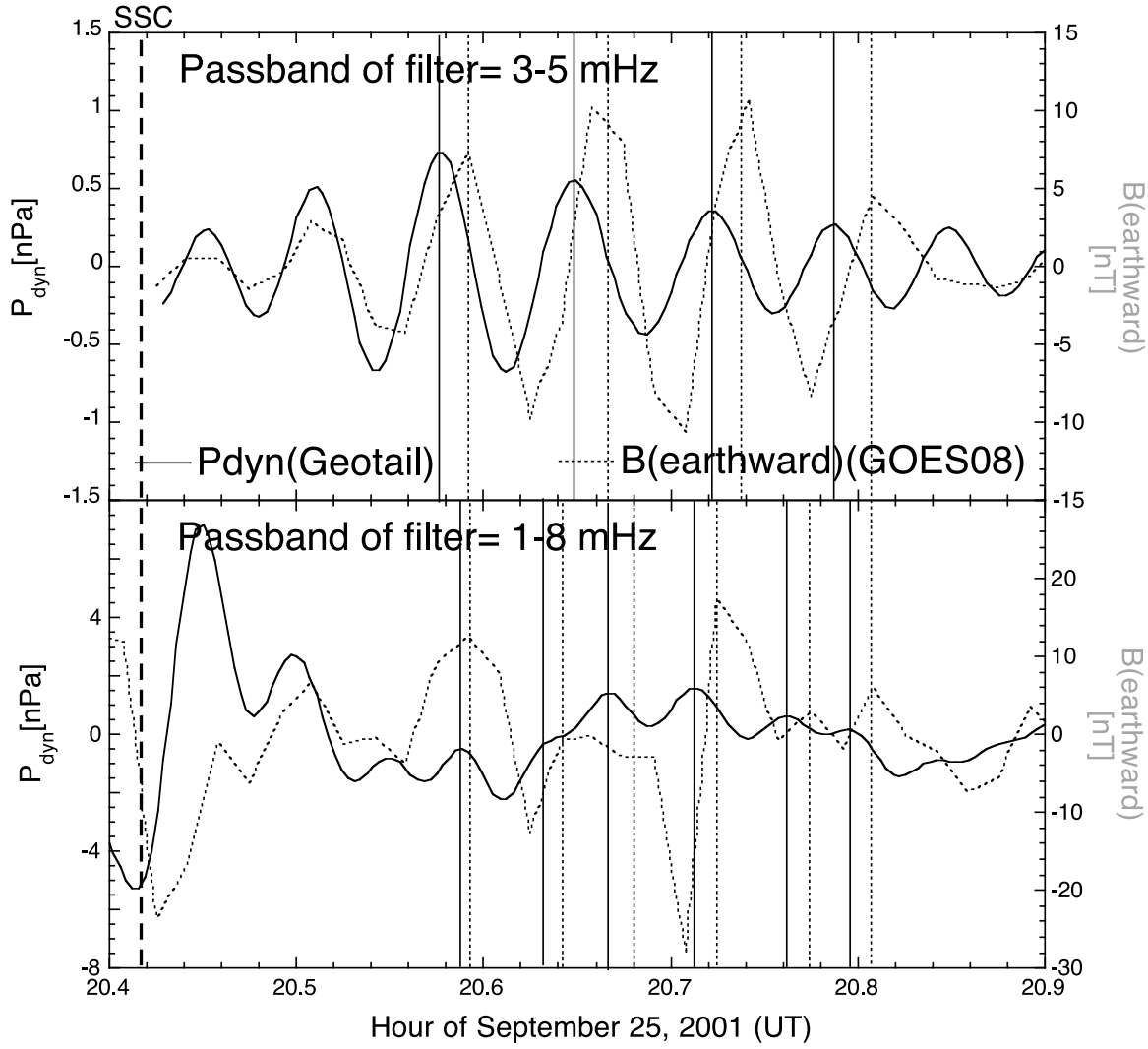

Figure 8. Time profiles of $P_{\rm dyn}$ measured by Geotail and B(earthward) measured by GOES 8. The vertical lines indicate the wave peak crossing time. (top) A narrowband (3–5 mHz) filter is used. (bottom) A broadband (1–8 mHz) filter is used.

tion of low-energy electron fluxes. In fact, the change in energy E_e of an electron moving adiabatically in electric and magnetic fields [*Northrop*, 1963] is

$$dE_e/dt = -e\,\mathbf{E}\cdot\mathbf{v_d} + M\;\partial B/\partial t, \tag{4}$$

where e is the electron charge, $\mathbf{v_d}$ is the electron drift velocity, and B is the magnetic field strength. Since the magnetic field component B_z of poloidal-mode waves is 90 degree out of phase with E_ϕ [e.g., *Takahashi et al.*, 2001], for an oscillatory $E_\phi \propto \cos(\omega_w t)$, where $\omega_w = 2\pi f_w$, there is a compressional-mode magnetic field component $B_z \propto \sin(\omega_w t)$ and $\partial B_z/\partial t \propto \cos(\omega_w t)$. The right-hand side of equation (4) is $\propto\cos(\omega_w t)$. Equation (4) then yields $\Delta E_e \propto \sin(\omega_w t)$, indicating a phase shift of $\pi/2$ between ΔE_e and E_ϕ. As an increase of ΔE_e would result in an increase of J_e measured by a fixed energy detector, the observed phase shift between J_e and E_ϕ can be explained. In contrast, Figure 8 (bottom) shows that high-energy (500–750 keV) electron flux peaks are not correlated with E_ϕ. Therefore, high-energy electron fluxes are not simply modulated by ULF waves, but experience anomalous energization by ULF waves [*Degeling et al.*, 2007], as shown in the next section. In *Zong et al.* [2007] and *Yang et al.* [2010], similar events of ULF wave modulation of much lower energy particle fluxes were reported from Cluster observations.

4.2. Acceleration of High-Energy Electrons

[41] From Figure 10 after SSC the sudden enhancement of electron fluxes is evident in the omnidirectional electron flux

Figure 9. Time profiles of the filtered E_y (first panel) and 30–100 keV electron fluxes (second panel) from Cluster-3. Time profiles of the electron fluxes at different energies from LANL91 are shown in the third through sixth panels. The vertical thin lines mark the times when E_y from Cluster-3 crosses zero from negative to positive. A broadband (1–8 mHz) filter is used.

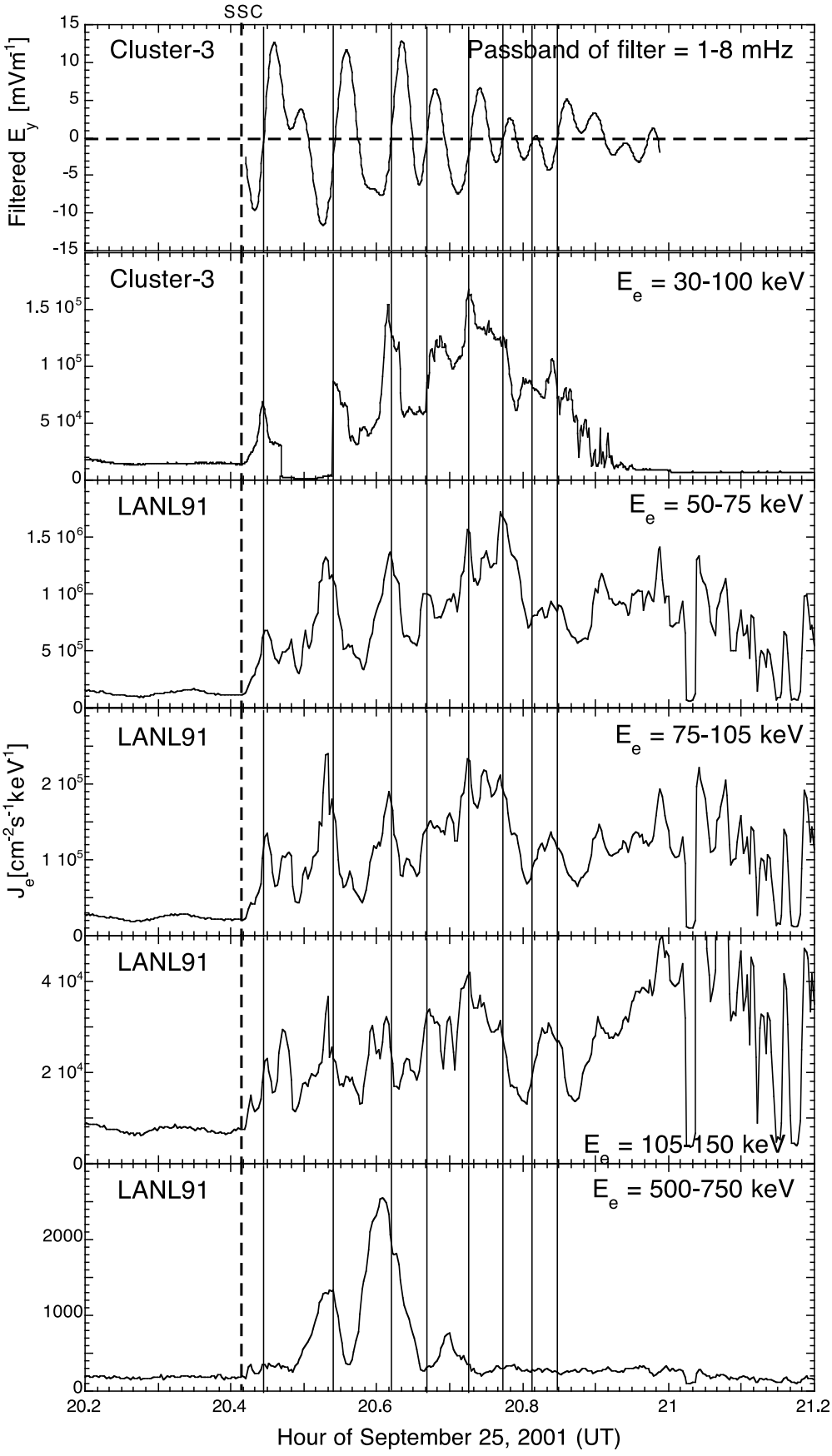
SSC
Cluster-3
Passband of filter = 1-8 mHz
Filtered E_y [mVm^{-1}]
Cluster-3
E_e = 30-100 keV
LANL91
E_e = 50-75 keV
LANL91
E_e = 75-105 keV
J_e[cm^{-2}s^{-1}keV^{-1}]
LANL91
E_e = 105-150 keV
LANL91
E_e = 500-750 keV
Hour of September 25, 2001 (UT)

Figure 9

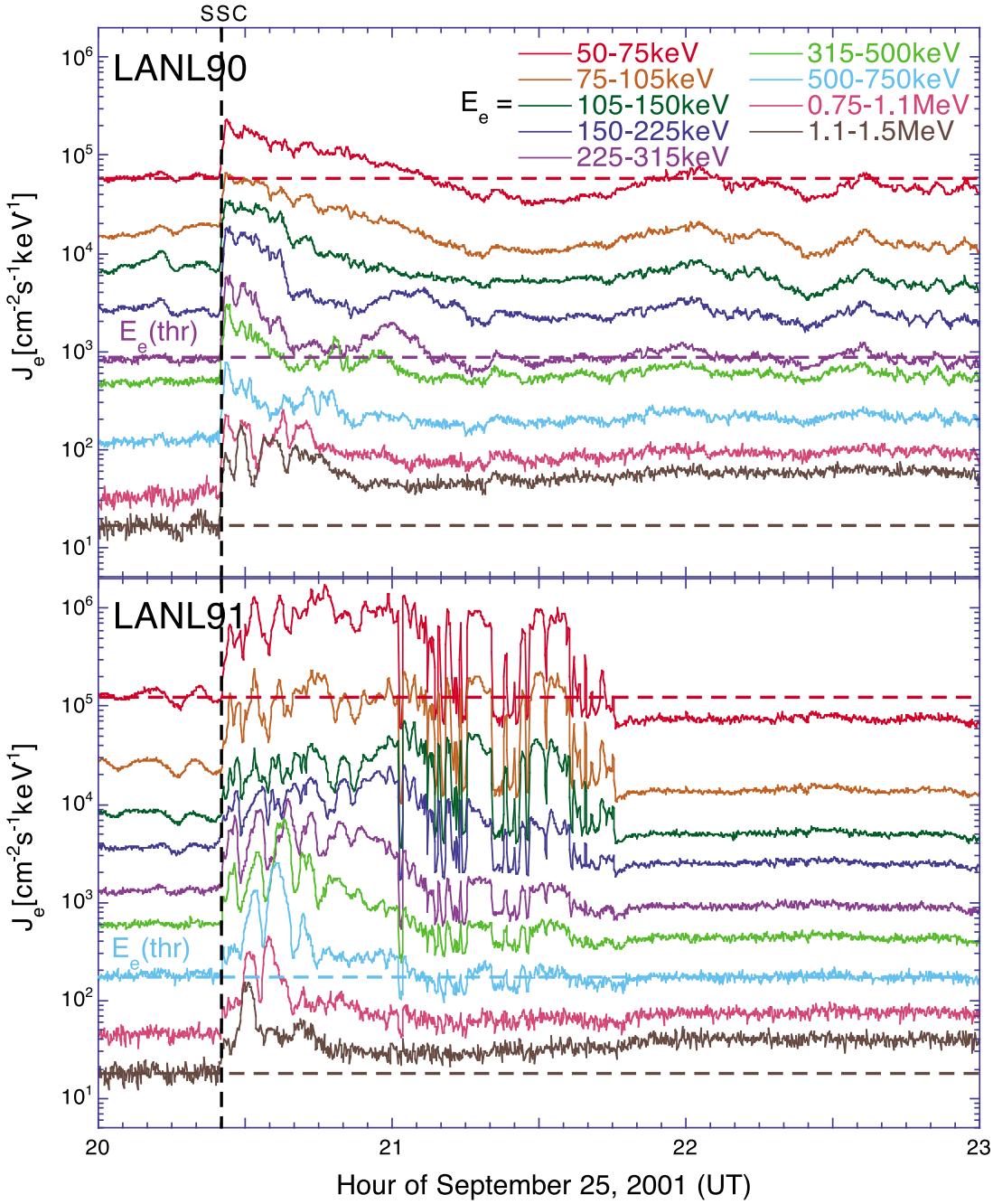

Figure 10. Time profiles of electron fluxes J_e measured by (top) LANL90 and (bottom) LANL91. In each panel the upper, middle, and lower horizontal dashed lines indicate the background J_e for E_e = 50–75 keV, $E_e = E_e$(thr), and E_e = 1.1–1.5 MeV, respectively.

J_e data measured by LANL90 located at dusk. It appears that the impulsive electron acceleration due to strong sudden dayside magnetosphere compression by fast interplanetary shocks, which is the sole cause in the 24 March 1991 SSC event [see *Blake et al.*, 1992; *Li et al.*, 1993], is also efficient for the dispersionless enhancement of electron fluxes near LANL90, because along the dusk flank the antisunward propagating waves could resonantly accelerate electrons (see section 3.3.4).

[42] It can be also seen from Figure 10 that during the first 1.5 h after SSC strong oscillation of low-energy (<500 keV) electron fluxes appeared on J_e data measured by LANL91 located near noon. However, such J_e oscillation cannot be explained as drift-echoes resulting from the J_e enhancement near LANL90, because (1) the calculated drift period of ~500 keV electrons starting from LANL91 is ~20 min that are significantly longer than the oscillation period of electron fluxes observed by LANL91 and (2) the electrons accelerated near LANL90, which is located at dusk, need to pass ~3/4 of drift period to reach LANL91 located near noon, while the observed electron enhancements appeared at LANL91 much earlier. As explained in section 4.1, the J_e

oscillation could be due to the low-energy electron modulation caused by ULF waves.

[43] In addition, from Figure 10 it can be seen that low-energy electrons did not have net energy increase in the two spacecraft observations, because J_e at the end of modulation (after 2140 UT) was lower than (for LANL91 in view of its multimagnetopause crossings) or nearly equal to (for LANL90) the preevent background value (the horizontal red line).

[44] On the other hand, after a fast oscillation of J_e during the first half hour after SSC, a steady enhancement of high-energy (e.g., 1.1–1.5 MeV) electron flux was observed until 2320 UT (also see Figure 2). Relative to the preevent background value, $J_e(E_e$ = 1.1–1.5 MeV) observed by LANL91 and LANL90 had a factor of 2.5 and 4 enhancements, respectively. There appeared to be an electron energy threshold E_e(thr), below which the electron fluxes are highly modulated by ULF waves and the final electron flux does not exceed the preevent background. Above E_e(thr) the electron flux increases steadily, showing a net gain. The threshold values E_e(thr) identified from LANL91 and LANL90 are shown in Figure 10 as the horizontal purple (300–500 keV) and blue (500–750 keV) lines.

[45] Furthermore, from Figure 10 it can be seen that there were large increases of high-energy electron fluxes with coherent fluctuations within ~1 h after SSC, which is consistent with the simulation by *Degeling et al.* [2007], showing that the time scale for anomalous energization is over the first ~15 wave periods, which is ~60 min for ULF wave frequency $f_w \sim 4$ mHz. Also, a steady high-energy electron flux increase occurred 1.5 h after SSC, which is also consistent with simulations [*Degeling et al.*, 2007] showing that the azimuthally averaged radial transport becomes diffusive over a time scale of ~25 wave periods. Thus the compressional-mode ULF waves are responsible for the acceleration of MREs in the event under study.

5. Analysis and Discussion

5.1. *L* Distribution of Equatorial Electric Field of ULF Waves

[46] What is the L range within which electrons can be effectively accelerated by ULF waves? Which wave mode (toroidal or poloidal) is more important in MRE acceleration? In order to answer these questions it is important to know the L distributions of both toroidal-mode (E_r) and poloidal-mode (E_ϕ) electric field components at the equator. It is difficult to determine these distributions from spacecraft observation, which usually covers only a limited L range.

[47] *Ozeke et al.* [2009] developed a technique to convert the magnetic field amplitudes of guided toroidal and poloidal waves observed on the ground into the equatorial electric field amplitudes of waves in space. According to their equation (24), the magnetic field amplitude observed at the top of ionosphere, b^i is

$$b^i_{\rm ob} = b^g_{\rm ob}[nT]\frac{1}{2}\exp\left(\left[m^2 \times L + \frac{4\pi^2}{(\Delta\theta[\text{radians}])^2}\right]^{1/2}\frac{100}{R_E[\text{km}]}\right), \tag{5}$$

where b^g is the magnetic field amplitude measured on the ground, m is the azimuthal wave number, $\Delta\theta$ is the full width half maximum (FWHM) of wave amplitude over a latitudinal array of magnetometers. Hereafter the subscript "ob" indicates an observed quantity. The equatorial electric field amplitude $E^{\rm eq}$ is approximately given by

$$E^{\rm eq}(f_w) = \frac{f_w[\text{mHz}]}{3}\left(\frac{E^{\rm eq}}{b^i}\right)_{3\ \text{mHz}} b^i_{\rm ob}, \tag{6}$$

where f_w is the frequency of ULF waves. In the work of *Ozeke et al.* [2009], the values of $(E^{\rm eq}/b^i)_{3\,\rm mHz}$ for the guided toroidal and poloidal-mode waves as a function of L under different field-aligned plasma density profiles are given in their Figure 5 (top and bottom), respectively.

[48] We calculate $E^{\rm eq}$ from the magnetic field data measured by the Fort Churchill line magnetometer array (see Figure 4 and the red dots in Figure 7). Because of the gap in magnetic field data measured by GILL, we use the interval 2230–2320 UT (i.e., between the two dash-dotted lines in Figure 4) to estimate b^g. Note that during this interval the Fort Churchill line (near the location of RABB in Figure 5, first panel) was near noon. In addition, during the time period of 2020–2120 UT Cluster-3 was also near noon, making it possible to compare the equatorial electric field data derived from the Fort Churchill line magnetometer measurements with that from Cluster-3 observations. While the Cluster-3 spacecraft was not exactly at the equator, the electric field measurements can be approximated to $E^{\rm eq}$ measured on its conjunction equatorial point (i.e., LANL91). This is because the electric field amplitudes of the fundamental-mode guided toroidal and poloidal waves remain almost constant along the magnetic field line [*Ozeke et al.*, 2009].

[49] In addition, when the wave observation in space is compared with that on the ground, it should be noted that the toroidal shear Alfvén wave in the magnetosphere is expected to be rotated through 90° upon transmission through a conducting ionosphere to the ground [*Hughes and Southwood*, 1976], thus the toroidal wave should be dominant in the B(northward) component of the ground-based magnetic field data. On the other hand, the dominant part of the poloidal-mode wave should be in the B(eastward) component of ground-based magnetic field data. Assuming that $\Delta\theta = \Delta\lambda/2 = 5.5°$ for the Fort Churchill line magnetometer array, we substitute $m = 3$ and $f_{\rm wob} = 4$ mHz into equations (7)–(8) to calculate $E^{\rm eq}$ of both toroidal and poloidal waves. In Figure 7 (bottom), the solid lines are $E^{\rm eq}$ deduced from the Fort Churchill line magnetometer measurements. The dashed lines show the error range, which takes into account of the following errors: (1) the error inherent in the broad band Pc-5 pulsations in the ground-based magnetic field data and (2) the error caused by assumptions on the field-aligned plasma density profiles ranging from $\propto 1/r$ to $\propto 1/r^5$. From Figure 7 (bottom), it can be seen that the electric field amplitudes measured by Cluster-3 and that deduced from the Fort Churchill Line magnetometer data are consistent. The L variation of $E^{\rm eq}$ deduced from the ground-based magnetometer data has the following features.

[50] 1. At $L < 6$ both E_r and E_ϕ amplitudes increase with increasing L, while at $L > 6$ a plateau in the amplitude is formed with a shallow maximum of amplitudes near L ~ 6.5.

The plateaus of both E_r and E_ϕ amplitudes at $L > 6$ imply that the electron acceleration can occur over a range of L values;

[51] 2. Within the plateau region the ratio E_r/E_ϕ is ~1.4. Nevertheless, the electron acceleration by E_ϕ should be more effective than by E_r. This is because E_r is perpendicular to the electron drift orbit and its energization effect depends on the drift orbit deviation Δr due to the magnetospheric compression. We can use a compressed dipole magnetic field to approximate the equatorial magnetic field configuration [*Elkington et al.*, 2003]. In this model the magnetic field strength B is a function of the radius r and azimuthal angle φ,

$$B(r, \phi) = b_0 + b_1(1 + b_2 \cos \phi), \tag{7}$$

where $b_0 = B_0 R_E^3/r^3$ ($B_0 = 3.11 \times 10^4$ nT), b_1 and b_2 are model parameters. Alternatively, we can introduce two new parameters $B_{\max} = b_0 + b_1(1 + b_2)$ and $B_{\min} = b_0 + b_1(1 - b_2)$ to describe the model, which correspond to day-night asymmetry in magnetic field configuration [*Tan et al.*, 2004]. For illustrative purposes, we may use $B_{\min} \sim 65$ nT and $B_{\max} \sim 190$ from the magnetic field B_z component measured by GOES 10 along its orbit on 25 September 2001 to conveniently set up the compressed dipole model. Thus the relative acceleration efficiency of E_r to E_ϕ can be related to the factor $\Delta r/r$ using the compressed dipole field model,

$$\Delta r/r \sim (b_{\max} - b_{\min})L^3/(6B_0), \tag{8}$$

which has a value of ~0.15 at $L = 6$ and ~0.49 at $L = 9$. Therefore, in the September event the electron acceleration is mainly due to the poloidal-mode electric field E_φ.

5.2. Cause of the Azimuthal Wave Number Differences of ULF Waves Between CARISMA and IMAGE Observations

[52] In section 3.3 the longitudinally distributed stations in the CARISMA and IMAGE magnetometer arrays are used to estimate the azimuthal wave number (m) of ULF waves at different local times (LTs). Using the ground-based magnetic field data filtered by a narrowband (3–5 mHz) filter, we find $m \sim 3$ and $m \sim 1$ at LT ~ 13 h (near noon) and LT ~ 22 h (near midnight), respectively (see Figure 5, first panel). Because the azimuthal wave number $k_\perp$ for an obliquely propagating compressional mode wave ($k_\perp \gg k_\parallel$) in the low beta plasma of the cold inner magnetosphere can be approximated by ω/V_A ($\approx \omega/V_{ph\perp}$) [e.g., *Boyd and Sanderson*, 2003] where ω and V_A are the angular frequency and local Alfvén speed, respectively, then at fixed ω the difference of m indicates that V_A near midnight should be 3 times of V_A near noon. It is interesting to explore the reason that causes such V_A difference.

[53] Using typical magnetospheric parameters at geosynchronous region ($\langle B \rangle \sim 140$ nT as measured by GOES 10 and $N \sim 104$ cm^{-3} at $L = 6$ as determined from a saturated dayside plasmasphere model [*Carpenter and Anderson*, 1992]), we obtain a rough estimate of the Alfvén speed to be ~ 300 km/s. It is noted that previous multisatellite observations [e.g., *Takahashi et al.*, 1984, and references therein] have indicated that the azimuthal propagation speeds $V_{ph\perp}$ of ULF waves can range from 300 km/s to 2500 km/s (Table 2 of *Takahashi et al.* [1984]). Our analyses show that the azimuthal phase velocity of compressional mode wave at $L \sim 6$ is ~ 280 km/s on the dayside, and ~ 1080 km/s on the midnight, consistent with the azimuthal phase velocity range observed by *Takahashi et al.* [1984]. This day-night difference can now be explained in terms of the change in $V_A \propto B/(N)^{1/2}$ in low beta plasma, where B and N are the local magnetic field strength and plasma density, respectively.

[54] In view of the use of a compressed dipole field model in section 5.1 above, if we assume that during the interval of interest the percentage difference between the dayside and nightside magnetic field strengths at $L \sim 6$ is much smaller than that between the corresponding densities, i.e., the departure of the magnetic field from a dipole configuration has less effect on the Alfvén speed [*Singer et al.*, 1981], then the observed local-time variation of V_A could be attributed to changes in plasma density (N) alone. In fact, the plasma density effect is related to the plasmapause variability, which is known to have a bulge in the afternoon sector. The bulge is caused by the drift of plasma in an electric field consisting of the corotation field and the dawn-to-dusk magnetospheric field.

[55] Since $V_{ph\perp} \approx V_A$ in the cold and low-beta plasma limits and $N \propto 1/V_A^2$, the factor-of-3 difference in $V_{ph\perp}$ (unrelated to the choices of compressed dipole model field parameters in section 5.1) indicates one order of magnitude difference in N between noon and midnight. In fact, because of upward flow from the ionosphere into depleted flux tubes, the plasmatrough region outside the plasmasphere exhibits readily detectable day/night differences in plasma density [*Carpenter and Anderson*, 1992; *Denton et al.*, 2006]. It is possible that the plasmatrough N level in the dayside is a factor of 5−10 higher than that in some nightside regions during the early phases of substorms [*Carpenter and Anderson*, 1992].

[56] The observed difference of m between the dayside and nightside is equivalent to a significant local time asymmetry of $m = 3$ harmonic component (see section 3.4). As explained in the next section, such asymmetry plays an important role in the energization of magnetospheric electrons by compressed mode ULF waves.

5.3. Electron Acceleration by Compressional-Mode ULF Waves

[57] To the first-order approximation, the symmetric drift resonance condition of electrons with the magnetic moment M to be resonantly interacting with ULF waves of the angular frequency ω_w in a dipolar magnetic field can be expressed as [e.g., *Elkington et al.*, 2003; *Degeling et al.*, 2007]

$$\omega_w = 3m_0 M/\left(\gamma e r^2 R_E^2\right), \tag{9}$$

where m is the azimuthal wave number, and γ is the relativistic correction factor

$$\gamma = \left(1 + 2MB(r)/\left(m_e c^2\right)\right)^{1/2}, \tag{10}$$

with m_e and c being the electron mass and the speed of light, respectively. Equation (9) can be rewritten as an equation for M:

$$\left(3m_0/\left(\omega_w e r^2 R_E^2\right)\right)^2 M^2 - \left(2B(r)/\left(m_e c^2\right)\right)M - 1 = 0, \tag{11}$$

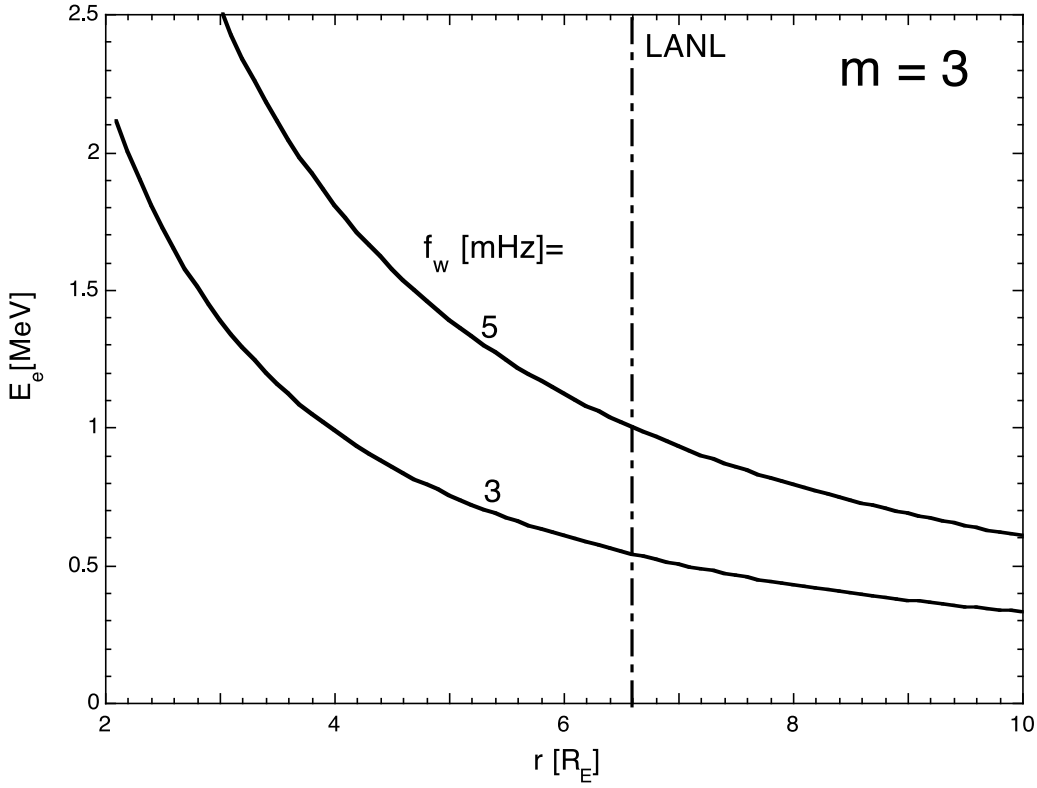

Figure 11. Energy E_e of electrons resonant with the ULF waves at frequencies f_w = 3 and 5 mHz and the azimuthal wave number m = 3 as deduced from equation (12).

which can be solved for the magnetic moment M of resonant electrons and hence their kinetic energy E_e. Note that equation (9) only considers single frequency ω_w and azimuthal wave number m, which is inconsistent with the broadband wave spectrum observed by us. Nevertheless, we wish to estimate the order of magnitude of E_e for accelerated electrons by using it.

[58] Since in the electric field PSD spectra measured by Cluster-3 (Figure 3, sixth panel) we observe broad peaks at 3 and 5 mHz, we hence calculate the r dependence of E_e for the wave frequency components f_w = 3 and 5 mHZ under the condition of m = 3 found from Figure 5. As shown in Figure 11, the predicted E_e range is between 0.5 and 1 MeV, which is qualitatively consistent with our observation shown in Figure 10. According to Figure 5, the ULF waves propagate eastward on the dusk side and westward on the dawnside in azimuthal direction. The electron acceleration is due to the drift-resonant acceleration of energetic electrons by eastward propagating ULF waves. Initially, LANL 91 only sees the electron flux modulation after the SSC. The flux increase observed by LANL 91 at later time is due to arrival of the drifting energetic electrons accelerated by drift-resonant acceleration at dusk side.

[59] In addition, *Degeling et al.* [2007] concluded that the azimuthal asymmetry of the compressional-mode ULF waves is an important factor determining the efficiency of the drift-resonant acceleration of magnetospheric electrons. Our observations are qualitatively consistent with their conclusion, although it is difficult to make a quantitative comparison of our broadband ULF wave observations with the single wave frequency model of *Degeling et al.* [2007]. In fact, while the wave amplitude measured by CARISMA in dayside is comparable to that by IMAGE at nightside, the azimuthal wave number $m \sim 3$ observed by CARISMA is different from $m \sim 1$ observed by IMAGE. The difference of m values suggests a significant asymmetric distribution of azimuthal wave component.

6. Summary

[60] Multiple spacecraft measurements and ground-based magnetometer data have been used to investigate the electron acceleration during the 25 September 2001 SSC event. Our main findings are as follows.

[61] 1. While the impulsive electron acceleration due to strong dayside magnetosphere compression by fast interplanetary shocks is still efficient to cause the initial sudden enhancement of electron fluxes, other acceleration mechanisms of electrons are necessary in order to account for the electron acceleration lasting ~3 h. This paper suggests that the magnetospheric electron acceleration by compressional-mode ULF waves is an important mechanism.

[62] 2. The observed magnetospheric and ground ULF waves can be excited by solar wind dynamic pressure fluctuations with the waves being driven by a continuous solar wind buffeting on the magnetosphere. A phase correlation is found between the solar wind dynamic pressure fluctuations and the magnetospheric poloidal-mode ULF waves. In addition, the electron acceleration interval coincides with the duration of the solar wind dynamical pressure pulsations.

[63] 3. The existence of compressional-mode ULF waves is confirmed through the comparison of the power densities of the magnetic field magnitude and total magnetic field. The equatorial electric field components of both toroidal and poloidal-mode waves are deduced from the CARISMA magnetometer data along the Fort Churchill line. The longitudinally distributed stations in the CARISMA and IMAGE magnetometer arrays are also used to estimate the wave propagation direction and the longitudinal location of solar wind buffeting on the magnetosphere.

[64] 4. We have identified the modulation of low-energy electrons and the acceleration of high-energy electrons by the poloidal-mode electric field oscillations. We have observed that the most significant electron acceleration occurred along the dusk flank, where the identified antisunward propagating waves could resonantly interact with the electrons. It is noted that the poloidal electric field component plays a dominant role in electron acceleration. The energy threshold of accelerated electrons at the geosynchronous orbit is ~0.4 MeV.

[65] 5. In addition, the longitudinally distributed stations in the CARISMA and IMAGE magnetometer arrays are used to estimate the azimuthal wave numbers (m) of ULF waves near noon and midnight, respectively. The significant difference of m values between noon and midnight indicate the presence of azimuthal asymmetry of the wave mode component of $m = 3$. The asymmetry could be a "hidden" factor affecting the magnetospheric electron acceleration.

[66] **Acknowledgments.** We acknowledge the use of data provided by the NASA/Space Physics Data Facility (SPDF) CDAWeb, Cluster, LANL, and IMAGE data centers. The authors thank I. R. Mann, D. K. Milling, and the rest of the CARISMA team for data. CARISMA is operated by the University of Alberta, funded by the Canadian Space Agency. We thank K. Papadopoulos (University of Maryland), I. Rae (University of Alberta), D. Vassiliadis (University of West Virginia), and M. K. Hudson (Dartmouth College) for fruitful discussions. We thank helpful comments from two referees. This work is partially supported by NASA grants NNX06AE88G and NNX07AF42G, ONR MURI grant N000140710789, and NSF grant ATM-0741841.

[67] Masaki Fujimoto thanks Biao Yang and another reviewer for their assistance in evaluating this paper.

References

Balogh, A., et al. (1997), The Cluster magnetic field experiment, *Space Sci. Rev.*, *79*, 65, doi:10.1023/A:1004970907748.

Belian, R. D., et al. (1992), High-Z energetic particles at geosynchronous orbit during the great solar proton event of October 1989, *J. Geophys. Res.*, *97*, 16,897, doi:10.1029/92JA01139.

Blake, J. B., et al. (1992), Injection of electrons and protons with energies of tens of MeV into $L < 3$ on 24 March 1991, *Geophys. Res. Lett.*, *19*, 821, doi:10.1029/92GL00624.

Boyd, T. J. M., and J. J. Sanderson (2003), *The Physics of Plasmas*, pp. 131–132, Cambridge Univ. Press, New York.

Carpenter, D. L., and R. R. Anderson (1992), An ISEE/whistler model of equatorial electron density in the magnetosphere, *J. Geophys. Res.*, *97*, 1097, doi:10.1029/91JA01548.

Degeling, A. W., et al. (2007), The effect of ULF compressional modes and field line resonances on relativistic electron dynamics, *Planet. Space Sci.*, *55*, 731, doi:10.1016/j.pss.2006.04.039.

Degeling, A. W., et al. (2008), Drift resonant generation of peaked relativistic electron distributions by Pc 5 ULF waves, *J. Geophys. Res.*, *113*, A02208, doi:10.1029/2007JA012411.

Denton, R. E., et al. (2006), Realistic magnetospheric density model for 29 August 2000, 2006, *J. Atmos. Sol. Terr. Phys.*, *68*, 615.

Elkington, S. R. (2006), A review of ULF interactions with radiation belt electrons, in *Magnetospheric ULF Waves: Synthesis and New Directions*, *Geophys. Monogr. Ser.*, vol. 169, edited by K. Takahashi et al., p. 177, AGU, Washington, D. C.

Elkington, S. R., M. K. Hudson, and A. A. Chan (1999), Acceleration of relativistic electrons via drift-resonant interaction with toroidal-mode Pc-5 ULF oscillations, *Geophys. Res. Lett.*, *26*, 3273, doi:10.1029/1999GL003659.

Elkington, S. R., M. K. Hudson, and A. A. Chan (2003), Resonant acceleration and diffusion of outer zone electrons in an asymmetric geomagnetic field, *J. Geophys. Res.*, *108*(A3), 1116, doi:10.1029/2001JA009202.

Gustafsson, G., et al. (1997), The Electric Field and Wave Experiment for Cluster, *Space Sci. Rev.*, *79*, 137, doi:10.1023/A:1004975108657.

Hughes, W. J., and D. J. Southwood (1976), The screening of micropulsation signals by the atmosphere and ionosphere, *J. Geophys. Res.*, *81*, 3234.

Kepko, L., H. E. Spense, and H. J. Singer (2002), ULF waves in the solar wind as direct drivers of magnetospheric pulsations, *Geophys. Res. Lett.*, *29*(8), 1197, doi:10.1029/2001GL014405.

Kim, K.-H., C. A. Cattell, D.-H. Lee, K. Takahashi, K. Yumoto, K. Shiokawa, F. S. Mozer, and M. Andre (2002), Magnetospheric responses to sudden and quasiperiodic solar wind variations, *J. Geophys. Res.*, *107*(A11), 1406, doi:10.1029/2002JA009342.

Kivelson, M. G. (2006), ULF waves from the ionosphere to the outer planets, in *Magnetospheric ULF Waves: Synthesis and New Directions*, *Geophys. Monogr. Ser.*, vol. 169, edited by K. Takahashi et al., p. 11, AGU, Washington, D. C.

Kokubun, S., et al. (1994), The GEOTAIL magnetic field experiment, *J. Geomagn. Geoelectr.*, *46*, 7.

Li, X., et al. (1993), Simulation of the prompt energization and transport of radiation belt particles during the March 24, 1991 SSC, *Geophys. Res. Lett.*, *20*, 2423–2426, doi:10.1029/93GL02701.

Mann, I. R., and A. N. Wright (1999), Diagnosing the excitation mechanisms of Pc5 magnetospheric flank waveguide modes and FLRs, *Geophys. Res. Lett.*, *26*, 2609, doi:10.1029/1999GL900573.

Mann, I. R., et al. (2008), The upgraded CARISMA magnetometer array in the THEMIS era, *Space Sci. Rev.*, *141*, 413–451, doi:10.1007/s11214-008-9457-6.

Mukai, T., et al. (1994), The low energy particle (LEP) experiment, onboard the GEOTAIL satellite, *J. Geomagn. Geoelectr.*, *46*, 669.

Northrop, T. G. (1963), *The Adiabatic Motion of Charged Particles*, Wiley-Interscience, New York.

Ogilvie, K. W., et al. (1995), SWE, a comprehensive plasma instrument for the WIND spacecraft, *Space Sci. Rev.*, *71*, 55, doi:10.1007/BF00751326.

Olson, J. V., and G. Rostoker (1978), Longitudinal phase variations of Pc 4–5 micropulsations, *J. Geophys. Res.*, *83*, 2481, doi:10.1029/JA083iA06p02481.

Ozeke, L. G., I. R. Mann, and I. J. Rae (2009), Mapping guided Alfvén wave magnetic field amplitudes observed on the ground to equatorial electric field amplitudes in space, *J. Geophys. Res.*, *114*, A01214, doi:10.1029/2008JA013041.

Rae, I. J., et al. (2005), Evolution and characteristics of global Pc5 ULF waves during a high solar wind speed interval, *J. Geophys. Res.*, *110*, A12211, doi:10.1029/2005JA011007.

Rème, H., et al. (2001), First multispacecraft ion measurements in and near the Earth's magnetosphere with the identical Cluster ion spectrometry (CIS) experiment, *Ann. Geophys.*, *19*, 1303, doi:10.5194/angeo-19-1303-2001.

Rostoker, G., et al. (1995), A ground-based instrument array for remote-sensing the high-latitude ionosphere during the ISTP/GGS programs, *Space Sci. Rev.*, *71*, 743, doi:10.1007/BF00751349.

Schulz, M., and L. J. Lanzerotti (1974), *Particle Diffusion in the Radiation Belts*, Springer, New York.

Singer, H. J., et al. (1981), Alfven wave resonances in a realistic magnetospheric magnetic field geometry, *J. Geophys. Res.*, *86*, 4589, doi:10.1029/JA086iA06p04589.

Singer, H. J., et al. (1996), Monitoring space weather with the GOES magnetometers, *SPIE Proc.*, *2812*, 299.

Takahashi, K., R. L. McPherrona, and W. J. Hughes (1984), Multispacecraft observations of the harmonic structure of Pc 3–4 magnetic pulsations, *J. Geophys. Res.*, *89*, 6758, doi:10.1029/JA089iA08p06758.

Takahashi, K., et al. (2001), CRRES observation of Pi2 pulsations: Wave mode inside and outside the plasmasphere, *J. Geophys. Res.*, *106*, 15,567, doi:10.1029/2001JA000017.

Tan, L. C., S. F. Fung, and X. Shao (2004), Observation of magnetospheric relativistic electrons accelerated by Pc-5 ULF waves, *Geophys. Res. Lett.*, *31*, L14802, doi:10.1029/2004GL019459.

Tan, L. C., et al. (2009), Observational evidence on the presence of an outer reflecting boundary in solar energetic particle events, *Astrophys. J.*, *701*, 1753, doi:10.1088/0004-637X/701/2/1753.

Tsyganenko, N. A. (1989), A magnetospheric magnetic field model with a warped tail current sheet, *Planet. Space Sci.*, *37*, 5, doi:10.1016/0032-0633(89)90066-4.

Vassiliadis, D., I. R. Mann, S. F. Fung, and X. Shao (2007), Ground Pc3–Pc5 wave power distribution and response to solar wind velocity time variations, *Planet. Space Sci.*, *55*, 743, doi:10.1016/j.pss.2006.03.012.

Villante, U., et al. (2006), ULF fluctuations of the geomagnetic field and ionospheric sounding measurements at low latitudes during the first CAWSES campaign, *Ann. Geophys.*, *24*, 1455, doi:10.5194/angeo-24-1455-2006.

Yang, B., Q.-G. Zong, Y. F. Wang, S. Y. Fu, P. Song, H. S. Fu, A. Korth, T. Tian, and H. Reme (2010), Cluster observations of simultaneous resonant interactions of ULF waves with energetic electrons and thermal ion species in the inner magnetosphere, *J. Geophys. Res.*, *115*, A02214, doi:10.1029/2009JA014542.

Zhu, X., and M. G. Kivelson (1988), Analytic formulation and quantitative solutions of the coupled ULF wave problem, *J. Geophys. Res.*, *93*, 8602, doi:10.1029/JA093iA08p08602.

Zong, Q.-G., et al. (2007), Ultralow frequency modulation of energetic particles in the dayside magnetosphere, *Geophys. Res. Lett.*, *34*, L12105, doi:10.1029/2007GL029915.

Zong, Q.-G., X.-Z. Zhou, Y. F. Wang, X. Li, P. Song, D. N. Baker, T. A. Fritz, P. W. Daly, M. Dunlop, and A. Pedersen (2009), Energetic electron response to ULF waves induced by interplanetary shocks in the outer radiation belt, *J. Geophys. Res.*, *114*, A10204, doi:10.1029/2009JA014393.

S. F. Fung, Geospace Physics Laboratory, NASA Goddard Space Flight Center, Greenbelt, MD 20771, USA.

X. Shao, A. S. Sharma, and L. C. Tan, Department of Astronomy, University of Maryland, College Park, MD 20742, USA. (xshaoup@yahoo.com)